Atomic resolution on the (111)*B* surface of mercury cadmium telluride by scanning tunneling microscopy

Fang-Xing Zha,[1,*] Feng Hong,[1,†] Bi-Cai Pan,[2] Yin Wang,[1] Jun Shao,[3] and Xue-Chu Shen[1,3]
[1]*Department of Physics and Laboratory for microstructures, Shanghai University, Shanghai 200444, China*
[2]*Key Laboratory of Strongly-Coupled Quantum Matter Physics, Department of Physics, University of Science and Technology of China, Hefei 230026, China*
[3]*Shanghai Institute of Technical Physics, Chinese Academy of Sciences, Shanghai 200083, China*

(Received 25 August 2017; revised manuscript received 13 November 2017; published 3 January 2018)

The real-space atomic surface structure of mercury cadmium telluride was successfully achieved on the (111)*B* surface of $Hg_{0.78}Cd_{0.22}Te$ by ultrahigh-vacuum scanning tunneling microscopy (STM). The work casts light on the reconstructions of the (111)*B* surface unraveling a (2×2) surface reconstruction induced by adatom adsorption of Cd. The other (2×2) surface reconstruction is clarified to be induced by the single Te vacancy, which is more stable than the reconstruction of multivacancies in contrast to the prevailing view. The simulated STM images are in good agreement with the experiments. We also observed an *in situ* morphology transition from the (1×1) structure to those (2×2) reconstructions, implying the stability of the reconstructions.

DOI: 10.1103/PhysRevB.97.035401

I. INTRODUCTION

The ternary compound mercury cadmium telluride (MCT, or $Hg_{1-x}Cd_xTe$) has been the most important semiconductor for infrared (IR) technology [1]. Recently, it has attracted further attention due to its close relationship with topological insulators (TI) [2–5]. However, the atomic surface structure of real space of the material has not been unveiled experimentally up to date. We report herein the development of the issue achieved by scanning tunneling microscopy (STM) with atomic resolution.

$Hg_{1-x}Cd_xTe$ has the same zinc-blende structure as CdTe or HgTe. It is generally viewed as a narrow-band-gap semiconductor with the energy band gap tunable from tens of meV to about 1 eV with the variation of composition [1,6]. However, when x is below the critical value (∼0.17), the semiconductor phase turns to the TI phase which is classified as a massless Kane-fermion system [5,7]. The surface property is an important issue for $Hg_{1-x}Cd_xTe$ and has been investigated with many conventional surface techniques such as reflection high-energy diffraction (RHEED) [1,8–12]. However, there are only a limited number of STM characterizations on the Cd(Hg)Te group in literature [13–19]. In particular, the STM work with atomic resolution on $Hg_{1-x}Cd_xTe$ has remained absent until now. It is in most extent due to the fact that the bond between Hg and Te atoms in $Hg_{1-x}Cd_xTe$ is weak in contrast to many semiconductors. It was indeed observed in our STM experiment that the surface atoms of HgCdTe manifest high mobility and the rearrangement of surface atoms could be induced easily by the STM tip during the imaging. The similar phenomenon was also noted in the previous STM on CdTe [14].

Nonetheless, the present STM experiment has succeeded in the atomic structure imaging on the (111)*B* surface of HgCdTe. The achievement illuminates a Cd-adatom-induced 2×2 reconstruction dominant for the (111)*B* surface, which was not shown previously. Employing the first-principles calculations, we elucidate that the 2×2 reconstruction induced by the single Te vacancy is energetically more stable than the widely referred multivacancies model [8,11], which was demonstrated for GaAs [20].

II. EXPERIMENTAL AND COMPUTATIONAL METHODS

The material for the STM experiment is a HgCdTe film about 15 μm thick, grown by liquid-phase epitaxy on the CdZnTe (111)*B* substrate. The HgCdTe surface also has the (111)*B* orientation, or noted as $(\bar{1}\bar{1}\bar{1})$ sometimes, which means that the growth direction is along [111] and the topmost layer is terminated by Te atoms. The orientation is commonly used in the epitaxy of HgCdTe since the direction entails the least Hg flux in comparison with the others [1]. The stoichiometry of Hg/Cd is 0.78/0.22, which is a typical ratio for the long-wavelength IR detectors and generates a band gap of ∼0.2 eV (300 K) [1,6]. For the STM characterization, the fresh surface was obtained through the following treatment: the sample was dipped into the 1% bromine/methanol for about 10 s followed by the subsequent rinsing with methanol and distilled water. It was then immediately dried with a stream of pure nitrogen gas. To avoid the oxidation in air, a thorough isolation process was available by using a home-built glove box, which can be sealed with the load-lock chamber so that the etching and transfer was manipulated in the nitrogen atmosphere. The pump-down with a turbo pump was then switched on and continued for 3 h before the sample transfer into the UHV. The instrument was the Omicron LT STM performed under ultrahigh vacuum with a base pressure of 1.0×10^{-10} mbar [21]. In the STM

*Corresponding author: fxzha@shu.edu.cn
†Corresponding author: fenghong@shu.edu.cn

experiment, we selected the sample bias within the range of $0.2 \sim 0.3$ V and the setpoint within $5 \sim 10$ pA.

To model the surface reconstructions, we applied the density-functional theory (DFT) calculation with the projector-augmented wave method implemented in the Vienna *ab initio* simulation package (VASP) [22,23]. The cutoff energy for the plane-wave basis set was 450 eV. In comparison with the local density approximation (LDA), the formalism of LDA + U introduces modification with the on-site Coulomb interaction [24]. The surface energy calculation presented was based on the LDA + U formalism with $U = 8.5$ eV. We also performed the LDA calculation to check the robustness on the prediction by LDA + U. Despite that the absolute values of surface energy calculated by LDA are about $1 \sim 4$ meV/Å^2 larger than those by LDA + U, we find that both conclusions have no difference and the use of U does not affect the relative stability. The surface was simulated with a slab consisting of eight bilayers with a composition of (Hg/Cd)-Te and vacuum thickness of 20 Å. The atoms in the bottom two bilayers were kept fixed at the bulk position, and those in upper bilayers were fully relaxed until the Hellmann-Feynman forces on them were smaller than 0.01 eV/Å. The dangling bonds of bottom cations were saturated by pseudohydrogen atoms. A $(5\times5\times1)$ k-point mesh was employed for (2×2) surface unit cell. The other details on calculation are shown in the next section.

The stability of the surface reconstructions are examined by their relative surface free energy with respect to that of pristine HgCdTe $(111)B$ surface,

$$\Delta\gamma = \frac{1}{A}\left[E_{\text{slab}}^{\text{recon}} - E_{\text{slab}}^{\text{ideal}} - \sum_i \Delta N_i\left(\Delta\mu_i + E_i^{\text{bulk}}\right)\right], \quad (1)$$

where $E_{\text{slab}}^{\text{recon}}$ and $E_{\text{slab}}^{\text{ideal}}$ are the total energy of the reconstruction and pristine $(111)B$ surface derived from a slab calculation, respectively; the integer ΔN_i indicates the number of atoms of type i that have been removed ($\Delta N_i < 0$) or added ($\Delta N_i > 0$) from the slab of the pristine surface to form the reconstructed structure, $\Delta\mu_i$ is the chemical potential of the ith element referring to the total energy E_i^{bulk} (eV/atom) of its most stable phase, and A is surface area. Determining the chemical potential under different growth condition is complicated due to the ternary alloy effect. In the present work, the chemical potential is simply evaluated from the formation enthalpy of CdTe [$\Delta H(\text{CdTe}) = -0.96$ eV] and HgTe [$\Delta H(\text{HgTe}) = -0.55$ eV] using virtual crystal approximation. Hence, the chemical potential of Te ($\Delta\mu_{\text{Te}}$) is $3/4\Delta H(\text{HgTe}) + 1/4\Delta H(\text{CdTe}) = -0.65$ eV under (Hg, Cd)-rich condition ($\Delta\mu_{\text{Hg}} = \Delta\mu_{\text{Cd}} = 0$). Under Te-rich condition ($\Delta\mu_{\text{Te}} = 0$), the chemical potential of Hg and Cd is also -0.65 eV.

III. RESULTS AND DISCUSSION

A. General features of STM images

A typical STM morphology is shown in Fig. 1(a), which displays mounds with the atomic flat terraces having the lateral dimension of tens of nanometers. Figure 1(b) shows a topography line profile measured across the steps as designated by the dashed line in Fig. 1(a). It indicates that the step height is about 0.37 nm, which is equal to the bilayer distance along [111] of HgCdTe. Figure 1(c) is a zoom-in image which

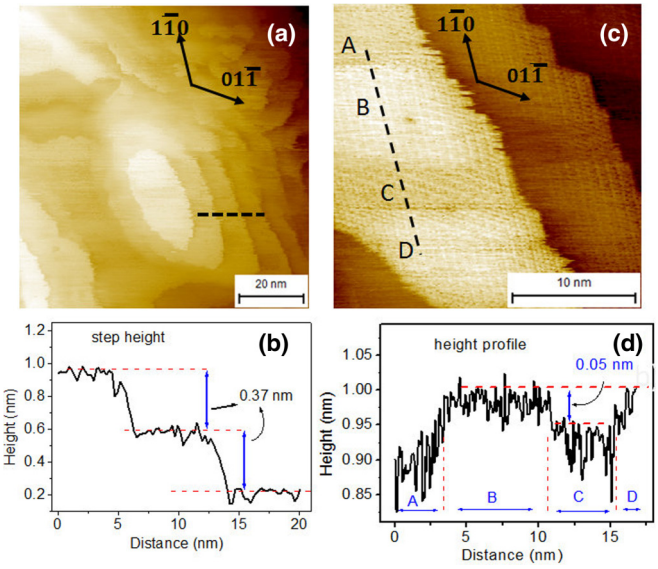

FIG. 1. STM images and topographic line profiles on $(111)B$ of HgCdTe acquired with the sample bias of 0.25 V and setpoint of 5 pA. A mound displays terraces with the step height of 0.37 nm as indicated by the line profile in (b). (c) Zoom-in image with two atomic flat terraces. The dotted line designates four reconstructed regions of A–D, for which the height variation is indicated by the line profile in (d).

displays four regions with different image contrast, as labeled with A/B/C/D. Figure 1(d) presents the height profile of the line across the regions. Note that the brighter regions of B and D are about 0.05 nm higher than region C, but region A is ~0.03 nm lower than C. The measurement uncertainty in the vertical direction is roughly ±0.005 nm and in the lateral is roughly ±0.04 nm. As indicated later, we resolved three types of atomic structures, for which B and D are induced by Cd adatom adsorption and C by the Te vacancy, respectively. Region A displays a type of (1×1) structure. The height variations reflect different normal relaxations of surface atoms with the reconstructions, as discussed in the text later.

Figure 2(a) presents the atomic resolution of a terrace, which displays two reconstructed areas as designated with the parallelogram (A) and rectangle (B), respectively. The A region contains a (2×2) reconstruction whose unit cell is a rhombus with the side length of ~0.96 (±0.04) nm. The region B displays the other (2×2) reconstruction for which the four vertexes of the unit cell are bright spots. The two regions differ slightly in height. For the dashed line designated in Fig. 2(a), its height profile is shown in (b) disclosing that the top atoms in the rectangle are about 0.05 nm higher than those in the parallelogram. Note in Fig. 1 that the height difference between the regions B and C is also of the same magnitude, implying the same reconstructions to which they belong.

Comparing the two reconstructions of A and B, we find two main differences: (i) the center of the unit cell of A is a hollow whereas the center of B is a bright spot; (ii) the two regions display different heights between which B is about 0.05 nm higher than A according to the eye guidance of two dashed lines drawn in Fig. 2(b). The reconstruction type of region B was also observed to have higher surface

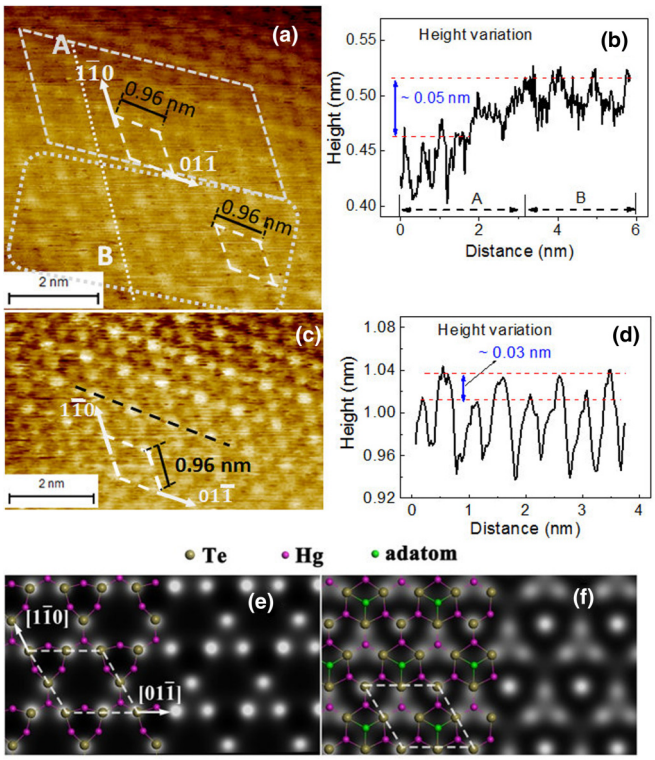

FIG. 2. Two typical (2×2) reconstructions of (111)*B* surface of HgCdTe. The STM images of (a) and (c) were acquired with the sample bias of 0.22 V and setpoint of 5 pA, respectively. In (a), two reconstructions are indicated with a parallelogram (A) and rectangle (B), respectively. The rhombus designates the unit cells. (b) Height profile for the dotted line across the regions A and B marked in (a). (c) The other high-resolution image with the same reconstruction as region B in (a). (d) is the height profile for the dashed line in (c). The comparable simulated STM images based on the DFT calculation are presented in (e) and (f). The color spots for different atom species are designated.

coverage than the others. Figure 2(c) presents the other image with improved resolution on the B reconstruction type. Figure 2(d) is the topographic line profile for the dashed line in (c), which indicates that the bright vertex spots of the unit cell are about 0.03 nm higher than the other atoms in the cell. The A- and B-type reconstructions can also be well reproduced by DFT simulation, results of which are displayed in Figs. 2(e) and 2(f). The details on the calculation as well as the comparison with Figs. 2(a) and 2(c) will be shown later in the text.

B. Calculation models and results

To elucidate the reconstructions, we resorted to the DFT calculation. In terms of the ternary compound $Hg_{1-x}Cd_xTe$, the construction of the model is quite complex due to the different permutations with two cations (Hg/Cd), which significantly affect the stability and electronic property. It is feasible to construct the model using $x = 0.25$ instead of the nominal $x = 0.22$ so that the composition of Cd and Hg for a supercell is treated succinctly with a ratio of 1:3. For $Hg_{0.75}Cd_{0.25}Te$, the energetic stability of the cation orderings was examined based on a (2×2×1) supercell (24 atoms) whose lattice vectors

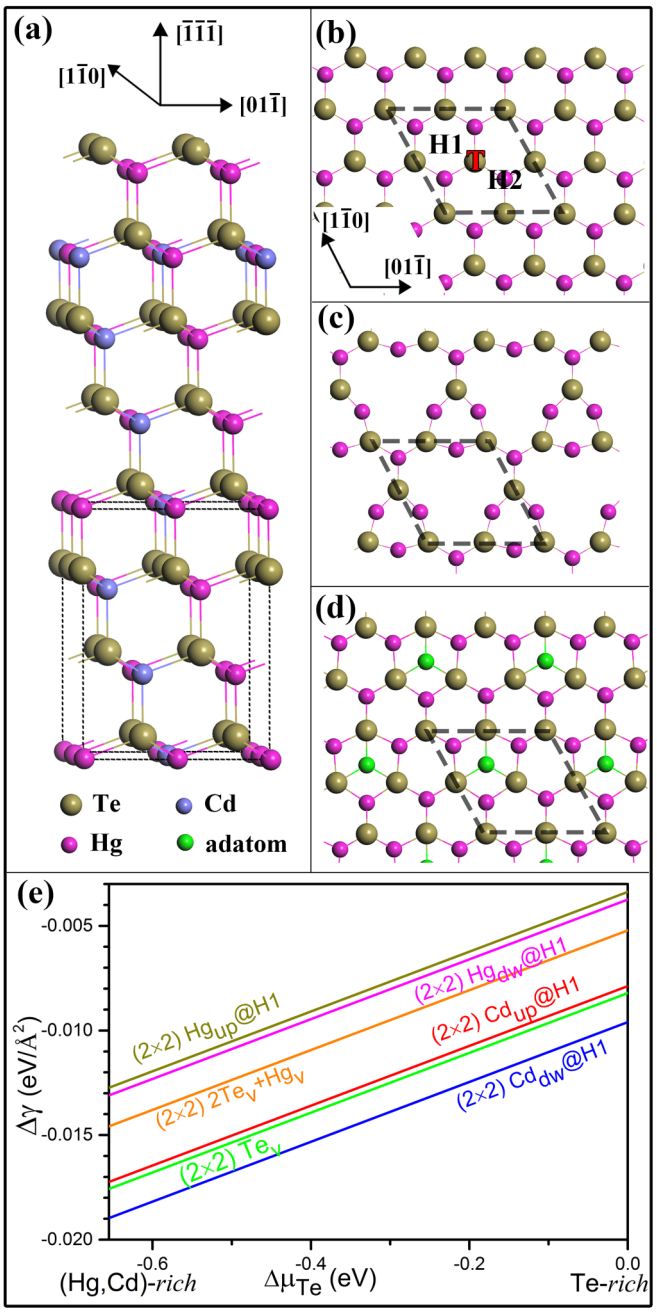

FIG. 3. Calculation models on $Hg_{0.75}Cd_{0.25}Te$ and the calculated surface energies of several reconstructions. (a) Side view of slab. The dashed frame indicates a supercell. The color spots for different atom species are designated. (b) Top view of (111)*B* surface. The dashed line marks a (2×2) surface unit cell. The notations H1, H2, and T designate three possible sites of the cation adsorption. (c), (d) Plots of (2×2) reconstructions induced by single Te vacancy (Te_v) and by Hg/Cd adatom at H1 site, respectively. (e) Surface energies calculated for the (2×2) reconstructions which are related to the (Hg/Cd) adatoms at H1 sites, Te_v, and multivacancies ($2Te_v + Hg_v$), respectively.

are along [1$\bar{1}$0], [01$\bar{1}$], and [$\bar{1}\,\bar{1}\,\bar{1}$], respectively. Figure 3(a) is a side view of a slab containing eight bilayers, and the dashed frame indicates (2×2×1) supercell mentioned above. We found totally 15 possible configurations for $Hg_{0.75}Cd_{0.25}Te$,

resulting from the different permutations of Hg/Cd atoms. Our calculation shows that these configurations have small difference in total energy, being less than 2 meV per formula unit. Hence, we can reduce the modeling complexity simply by using one supercell as a prototype of the slab model.

Realizing that the surface is likely to have a different chemical composition from the bulk, we need firstly clarify the favorable permutation of the cations (Hg/Cd) for the surface. The calculation was performed with the different distributions of two Cd and six Hg atoms in the two bilayers on top. Using the ratios of 0:4, 1:3, and 2:2 for Cd and Hg of the surface, we find that the total energy with the ratio of 0:4 is about 0.1 eV per (2×2) cell smaller than the others. The result implies the pure phase segregation of HgTe on the surface, in accordance with the previous study by the other approach [25]. This configuration was then used as the pristine surface for further investigation of the surface reconstruction.

In many cases, the reconstructions of a semiconductor surface obey the so-called electron counting rule (ECR), predicting that the electronic structure of the reconstructed surface should be nonmetallic [26]. In terms of the (111)B surface of a zinc-blende structure, there are two vacancy types of (2×2) reconstructions reported previously. For HgTe (111)B surface, the single vacancy type is formed by removing one Te atom for every (2×2) cell [8] and we denote this configuration herein as Te_v. Another multivacancy (2×2) type is formed by removing two Te and one Hg for every (2×2) cell [20], which we denote as (2×2)$2Te_v + Hg_v$. We point out that both the above vacancy configurations are conformed to ECR. In the present work, we reveal that there exists the other adatom type (2×2) reconstruction, which does not only satisfy ECR but also displays even lower surface energy than those vacancy (2×2) types. The description is given below.

The adatom type is formed in such a way that an adatom of cation (Cd or Hg) is adsorbed for every (2×2) cell. For this type, three adsorbed sites are involved, including one site on top of a surface Te atom denoted T in Fig. 3(b) and two hollow sites denoted H1 and H2. The notation H2 refers to the adatom directly on top of a surface Hg atom. The adatom at H1 is threefold coordinated with Te atoms [see Fig. 3(d)] and it also faces downward to a "full hollow" position so that the adatom has a possibility to diffuse into the bilayer. We distinguish the two configurations of the H1 site with the notations $Cd(Hg)_{up}$@H1 and $Cd(Hg)_{dw}$@H1, respectively. The single Te vacancy model is illustrated by Fig. 3(c) and the model of the above adatom configurations is illustrated by Fig. 3(d), in which the green spot represents the adatom.

Figure 3(e) presents the calculation results of surface energy which is a function of chemical potential of Te ($\Delta\mu_{Te}$). The plot shows that Cd_{dw}@H1 is the most stable configuration and Cd_{up}@H1 may transform to the more stable Cd_{dw}@H1 through the diffusion of adatom downward if the adatom initially stayed above the surface. Among the three cation-adsorption sites (H1, H2, and T), our calculation shows that the H1 site is energetically lower than the other two sites (H2 and T). For instance, the calculation indicates that the surface energy of Hg_{dw}@H1 configuration is 0.11 eV/(2×2) cell and 0.08 eV/(2×2) cell lower than that of Hg@H2 and Hg@T, respectively. Thus, the energy levels for the H2 and T sites are not put together in Fig. 3(e) for conciseness of the diagram. In terms of the vacancy-induced (2×2) reconstructions, Fig. 3(e) shows that both Te_v and $2Te_v + Hg_v$ reconstructions have lower surface energy than the pristine surface. The vacancy reconstruction models on (111)B surface of zinc-blende structure were initially addressed on GaAs by Chadi [20], who showed that the (2×2) reconstruction of $2As_v + Ga_v$ is more stable than that of As_v. The conclusion therein was later referred by the other studies on the zinc-blende structures including the Cd(Hg)Te group [8,11]. To the authors' knowledge, the adequacy of the extension has not been justified by the first-principles calculations until now. Our result shown in Fig. 3(e) indicates that the energy order of the two types of vacancy models for HgCdTe is contrary to that on the counterparts of GaAs. Namely, the Te_v (2×2) reconstruction is more stable than that of $2Te_v + Hg_v$. Additionally, the $2Te_v + Hg_v$ reconstruction was not yet observed by the STM.

C. Comparison between calculation and experiment

Figures 2(e) and 2(f) present the simulation results on the STM images based on the DFT calculation. Since the measured STM images were acquired with the positive sample bias, the tunneling current arises from the electron transport from the STM tip to the empty states of sample surface. The calculation has taken into account the total density of empty states at the bottom of conduction band (E_c), which is integrated over the energy range of $E_c \sim E_c + 0.2$ eV. The simulated images in Fig. 2(e) and 2(f) reflect the spatial distribution of empty charge states at the height of 0.2 nm above the surface. We find that the bright contrast arises mainly from the empty states of topmost Te atoms. Figures 2(e) and 2(f) are well compared with the STM measurements of Figs. 2(a) and 2(c), respectively.

Precisely speaking, Figs. 2(e) and 2(f) should be viewed as the STM images based on the acquisition of constant height mode rather than the constant current mode. Since the constant current imaging mode was practically used by our instrument, one should also take into account the vertical relaxation of surface atoms to fully interpret the STM contrast. Our calculation reveals that the reconstructions discussed previously are associated with appreciable relaxations of the surface atoms. For the case of $Cd(Hg)_{dw}$@H1, the topmost layer is Te terminated, which can be classified into two site groups. One group of Te atoms with a unit cell consists of the three Te atoms bonding to the Cd adatom, which move upward by 0.012 nm from the ideal case, whereas another group is the other Te atom which moves upward by 0.053 nm. Hence, their height difference between the two site groups of Te is 0.041 nm, close to the experimental value indicated in Fig. 2(d), which is ~0.03 nm as measured by the average height difference between the bright vertex spots and the other darker ones.

The calculation also provides the comparison of vertical relaxation between the different reconstructions. For the Te_v (2×2) reconstruction, the surface Te and Hg atoms move upward and downward from the original ideal case by 0.024 and 0.007 nm, respectively. In contrast, the surface Te atoms in the Cd_{dw}@H1 (2×2) case move upward by 0.053 nm so that the topmost layer of the Cd_{dw}@H1 (2×2) should be 0.029 nm higher than that of Te_v (2×2). The value is

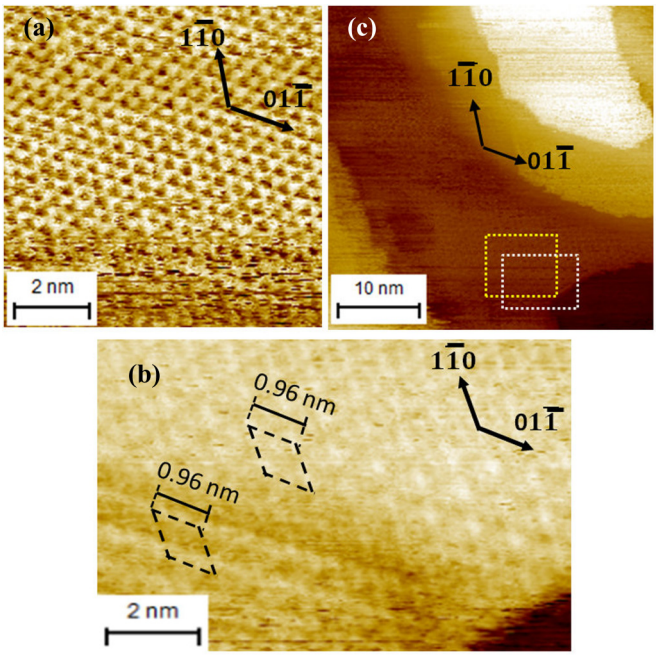

FIG. 4. Morphology transition observed with the STM acquired with the sample bias of 0.22 V and setpoint of 5 pA. (a) A (1×1) surface structure initially observed. (b) Image after several imaging cycles subsequent to (a). Two reconstructions can be resolved, which are the reconstructions due to Cd adatom and single Te vacancy, respectively. (c) Zoom-out image indicating large overlap between the two image areas in (a) and (b).

reasonably comparable with the measured ~0.05 nm indicated in Fig. 2(b) as well as in Fig. 1(d) while the influence of other factors such as the local density of states and tip geometry has not been taken into account.

D. Observation of (1×1) structure and its transformation to (2×2) reconstruction

We also observed a (1×1) structure, as shown in Fig. 4(a). However, the (1×1) structure did not survive with a long time repeated imaging. Note that the frame of image in Fig. 4(a) displays the blurred morphology at the lower part. The image in Fig. 4(b) was acquired later roughly in the same area as that for Fig. 4(a). The spatial relationship of the two imaging areas for Figs. 4(a) and 4(b) can be further illustrated with the zoom-out image in Fig. 4(c), in which the overlapped region had displayed the (1×1) structure in the very beginning. The subsequent image in Fig. 4(b) contains two reconstructions which redisplay those structures shown in Fig. 2(a). The phenomenon implies that the two (2×2) reconstructions are energetically stable, in accordance with the previous prediction by the surface energy calculation.

Generally, the reconstruction with lowest surface energy should be most favorable. Indeed, the Cd-adatom-induced (2×2) reconstruction is the most commonly observed surface structure, whose surface coverage by rough estimation is about 70%, whereas the coverage of (2×2) Te_v and (1×1) structures together are less than 30%. Regarding Fig. 3(e), one might question why it is possible to observe the reconstructions with different surface energies simultaneously. We remind that the approach used to calculate Fig. 3(e) is essentially a simplified treatment, which has assumed the same global chemical environment for an ideal surface. Practically, the local chemical environment such as the atom species and numbers with respect to a specific surface location may deviate from the ideal case leading to spatially different reconstructions. Once the reconstruction forms, it is metastable. The energy barrier may exist preventing the spontaneous transformation to the other lower energetic type, unless the lattice bonding could be broken by an external disturbance such as the tip-surface interaction in the STM or the high-energy electrons with the RHEED measurement.

In fact, the coexistence of different reconstructions was also observed by some other STM experiments. For instance, in both STM studies of CdTe(001) and HgTe(001) surfaces, the STM with atomic resolution revealed the mixed reconstructions of c (2×2) and (2×1) [14,16]. The other experiment by the RHEED technique revealed that the (1×1) structure of (111)B can indeed stand alone but the high-energy electron beam with the RHEED measurement eventually induced the structure transformation to the other $2\sqrt{3}\times 2\sqrt{3}R30^\circ$ reconstruction [10]. In our STM experiment herein, the (1×1) structure is of similar metastable feature. The eventual transformation to the (2×2) reconstruction may have been induced by the tip- surface interaction in contrast to the high-energy electrons in RHEED shown in Ref. [10]. In addition, we mention that the $2\sqrt{3}\times 2\sqrt{3}R30^\circ$ was the other reconstruction observed for (111)B of CdTe [11]. However, Duszak *et al.* showed that $2\sqrt{3}\times 2\sqrt{3}R30^\circ$ was observed above 310 °C, below which the reconstruction vanished and the (1×1) and (2×2) reconstructions occurred instead [11]. Nevertheless, we do not exclude the possibility of other reconstructions which could be probed by the STM exploration in the future.

Regarding the interference of high mobility of surface atoms on stable STM imaging, one might expect to ameliorate the effect with the low-temperature measurement. Although we performed the experiment at liquid nitrogen (77 K), we did not succeed to acquire atomic resolution. The failure may be due to the following fact. Since the narrow-band-gap semiconductor is concerned, the temperature affects sensitively the concentration of free carriers of the semiconductor, which drops drastically by several orders when the temperature changes from RT to 77 K [1]. The stable STM imaging is difficult due to poor carrier concentration, as observed by other STM experiments [27]. We also found that it was difficult to obtain atomic resolution with the negative voltage bias due to the large band-bending effect with the reverse bias [28].

IV. CONCLUSION

The real-space imaging on atomic structure of MCT surface is successfully demonstrated by the present STM work. Among the observed surface structures, the (2×2) reconstruction induced by the Cd adatom is most favorable energetically. Along with the first-principles calculations, the STM study shows that the (2×2) reconstruction induced by the single Te vacancy is more stable than that by multivacancies. We

had also observed a metastable (1×1) structure which was transformed to the more stable (2×2) reconstructions. The success demonstrated by the present experiment paves the way for further STM characterizations at the atomic level, which are not only promising for clarifying the crucial defect issues for the device physics but also for providing significant insight into TI on account of the uniqueness of $Hg_{1-x}Cd_xTe$ which inherently bridges the two phases of normal semiconductor and TI.

ACKNOWLEDGMENTS

The work is supported by Grant No. 61474073 of National Natural Science Foundation of China and partly supported by National Basic Research Program of China (Grant No. 2014CB 643900). We are grateful to Jianrong Yang for helpful discussions and thank Songmin Zhou and Rongshui Yu for assistance in the experiment. The calculations were performed on the high-performance computing platform of Shanghai University.

[1] P. Capper and G. James, *Mercury Cadmium Telluride: Growth, Properties and Applications* (John Wiley and Sons, West Sussex, 2010).
[2] M. König, S. Wiedmann, C. Brüne, A. Roth, H. Buhmann, L. Molenkamp, X.-L. Qi, and S.-C. Zhang, Science **318**, 766 (2007).
[3] M. Z. Hasan and C. L. Kane, Rev. Mod. Phys. **82**, 3045 (2010); X. L. Qi and S. C. Zhang, *ibid.* **83**, 1057 (2011).
[4] F. Virot, R. Hayn, M. Richter, and J. van den Brink, Phys. Rev. Lett. **111**, 146803 (2013).
[5] M. Orlita1, D. M. Basko, M. S. Zholudev, F. Teppe, W. Knap *et al.*, Nat. Phys. **10**, 233 (2014).
[6] G. L. Hansen, J. L. Schmit, and T. N. Casselman, J. Appl. Phys. **53**, 7099 (1982).
[7] J. W. Nicklas and J. W. Wilkins, Phys. Rev. B **84**, 121308(R) (2011).
[8] M. Seelmann-Eggebert, in *Properties of Narrow Gap Cadmium-Based Compounds*, edited by P. Capper (INSPEC, Institution of Electrical Engineers, London, 1994).
[9] S. Sivananthan, X. Chu, J. Reno, and J. P. Faurie, J. Appl. Phys. **60**, 1359 (1986).
[10] Y. S. Wu, C. R. Becker, A. Waag, M. M. Kraus, R. N. Bicknell-Tassius, and G. Landwehr, Phys. Rev. B **44**, 8904 (1991).
[11] R. Duszak, S. Tatarenko, J. Cibert, N. Magnea, H. Mariette, and K. Saminadayar, Surf. Sci. **251**, 511 (1991).
[12] J. Ren, L. Fu, G. Bian, M. Wong, T. Wang, G. Zha, W. Jie, T. Miller, M. Z. Hasan, and T.-C. Chiang, Phys. Rev. B **91**, 235303 (2015).
[13] C. K. Egan, Q. Z. Jiang, and A. W. Brinkman, J. Vac. Sci. Technol. A **29**, 0110211 (2011).
[14] L. Seehofer, V. H. Etgens, G. Falkenberg, M. B. Veron, D. Brun *et al.*, Surf. Sci. **347**, L55 (1996).
[15] L. Seehofer, G. Falkenberg, R. L. Johnson, V. H. Etgens, S. Tatarenko, D. Brun, and D. Daudin, Appl. Phys. Lett. **67**, 1680 (1995).
[16] S. Oehling, M. Ehinger, T. Gerhard, C. R. Becker, G. Landwehr *et al.*, Appl. Phys. Lett. **73**, 3205 (1998).
[17] S. Oehling, M. Ehinger, W. Spahn, A. Waag, C. R. Becker, and G. Landwehr, J. Appl. Phys. **79**, 748 (1996).
[18] F. X. Zha, M. S. Li, X. R. Ren, Q. Y. Wang, J. Shao, K. An, X. L. Zhao, and X. C. Shen, Appl. Phys. Lett. **101**, 141604 (2012).
[19] G. Panin, C. Díaz-Guerra, and J. Piqueras, Appl. Phys. Lett. **72**, 2129 (1998).
[20] D. Chadi, Phys. Rev. Lett. **57**, 102 (1986).
[21] F. Shao, F. X. Zha, C. B. Pan, J. Shao, X. L. Zhao, and X. C. Shen, Phys. Rev. B **89**, 085423 (2014).
[22] P. E. Blöchl, Phys. Rev. B **50**, 17953 (1994); G. Kresse and D. Jouber, *ibid.* **59**, 1758 (1999).
[23] G. Kresse and J. Furthmüller, Phys. Rev. B **54**, 11169 (1996).
[24] J. Li, N. Kioussis, F. Aqariden, and C. Grein, Phys. Rev. B **85**, 235306 (2012).
[25] R. S. Patrick, A.-B. Chen, A. Sher, and M. A. Berding, Phys. Rev. B **39**, 5980 (1989).
[26] M. D. Pashley, Phys. Rev. B **40**, 10481 (1989).
[27] F. Flores and N. Garcia, Phys. Rev. B **30**, 2289(R) (1984).
[28] N. D. Jäger, Ph. Ebert, K. Urban, R. Krause-Rehberg, and E. R. Weber, Phys. Rev. B **65**, 195318 (2002).